Layer-dependent zero-line modes in antiferromagnetic topological insulators

Wenhao Liang [ORCID],[1] Tao Hou [ORCID],[1,2] Junjie Zeng,[1] Zheng Liu,[1] Yulei Han [ORCID],[3,*] and Zhenhua Qiao [ORCID][1,4,†]

[1]*Department of Physics, and CAS Key Laboratory of Strongly-Coupled Quantum Matter Physics,*
University of Science and Technology of China, Hefei, Anhui 230026, China
[2]*Division of Physics and Applied Physics, School of Physical and Mathematical Sciences,*
Nanyang Technological University, Singapore 637371, Singapore
[3]*Department of Physics, Fuzhou University, Fuzhou, Fujian 350108, China*
[4]*ICQD, Hefei National Research Center for Physical Sciences at the Microscale,*
University of Science and Technology of China, Hefei, Anhui 230026, China

Recently, the magnetic domain walls have been experimentally observed in antiferromagnetic topological insulators $MnBi_2Te_4$. Here we study the intrinsic topological zero-line modes (ZLMs) that appear along the domain walls, and find that these ZLMs are layer dependent in $MnBi_2Te_4$ multilayers. We reveal the role of the spatial layer degree of freedom and magnetic domain wall configurations in determining the electronic transport properties and the distribution of the ZLMs in antiferromagnetic topological insulator systems. For antiferromagnetic domain wall with out-of-plane magnetization within each domain, we find that ZLMs are only distributed in the odd-number layers equally. For the Néel domain wall, the ZLMs are no longer distributed in the odd-number layers equally due to the mirror symmetry (M_z) breaking, and can exist in the even-number layers in multilayer systems. Moreover, the ZLMs are mainly distributed in the outermost layers with increasing layer thickness. Our findings lay out a strategy in manipulating ZLMs and can be utilized to distinguish the corresponding magnetic structures.

I. INTRODUCTION

The topological ZLMs that result from the reversal of mass signs [1], also known as topological confinement [2] or kink states [3,4], appear along the interface between two topological nontrivial regions with different topologies, e.g., quantum valley Hall insulators with different valley Chern numbers [5], quantum anomalous/valley Hall systems [6], quantum spin/valley Hall systems [7], and quantum anomalous Hall insulators with different Chern numbers [8]. It has been widely explored in graphene-like systems [9–16] and experimentally demonstrated that it can be modulated by external fields [17–19] or the domain wall structures [20,21]. Inspired by recent experimental discovery of layer Hall effect in topological axion antiferromagnets [22], we predict that the spatial degree of freedom corresponding to different layers is an efficient method to manipulate the ZLMs.

Intrinsic antiferromagnetic topological insulator $MnBi_2Te_4$ [23–38] has attracted intense interest recently since it bridges the fields of topology, magnetism, and van der Waals materials, where the neighboring ferromagnetic Mn layers are coupled in an antiparallel manner displaying A-type antiferromagnetism. The unique layer degree of freedom of this van der Waals material exhibits significant influence on topological phases, e.g., topologically trivial insulator in monolayer, Chern insulator in the odd-number layers ($n > 1$), and axion insulator in the even-number layers [31]. Moreover, when the temperature is below the Néel ordering temperature, the antiferromagnetic domain walls have been experimentally observed in layered $MnBi_2Te_4$ [32], which provides an ideal natural platform to investigate the effect of layer degree of freedom on ZLMs. Despite there are some studies on the magnetic domain walls recently [39–44], the exploration of the effect of layers on ZLMs in interlayer antiferromagnetic topological insulators remains scarce.

In this article, we systematically study the electronic transport properties of $MnBi_2Te_4$ multilayers with various magnetic domain walls. For antiferromagnetic domain walls with out-of-plane magnetization within each domain, we find that the counter-propagating chiral ZLMs along domain walls and quantum anomalous Hall edge states along boundaries coexist with double degeneracy, leading to quantized conductance of $2\ e^2/h$. The ZLMs and edge states are only distributed in the odd-number layers, displaying layer-dependent features. When the magnetic domain wall is a Néel domain wall, the ZLMs are no longer equally distributed in the odd-number layers due to M_z symmetry breaking, and can also exist in the even-number layers in multilayer systems. And which layer the ZLMs are mainly distributed in depends on the specific configuration if the Néel domain wall is clockwise or anticlockwise. Furthermore, with increasing layer thickness, the ZLMs are mainly distributed in the outermost layers. Meanwhile, the ZLMs in our article are intrinsic, requiring no external fields.

The rest of the paper is organized as follows. In Sec. II, we introduce the model Hamiltonian and electronic transport calculation methods. In Sec. III, we explore the topological and electronic transport properties of the three-layer system

*Correspondence author: han@fzu.edu.cn
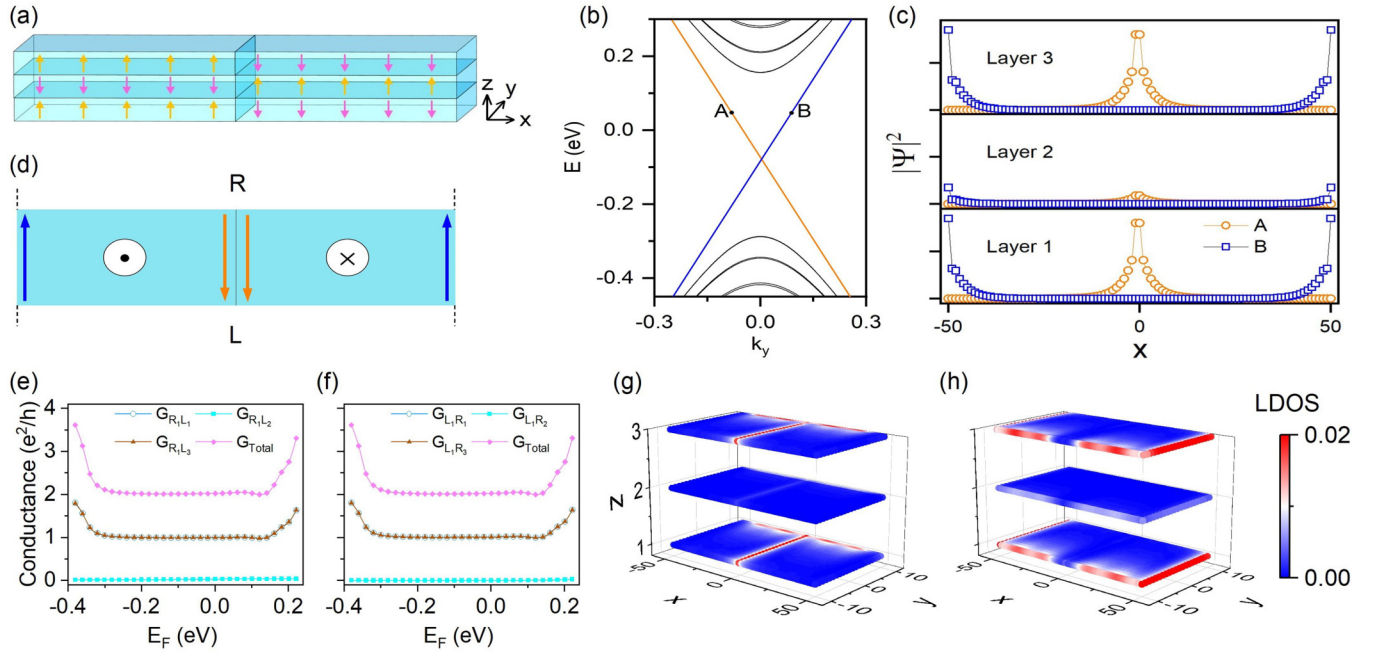†Correspondence author: qiao@ustc.edu.cn

FIG. 1. (a) Front view of the three-layer antiferromagnetic domain-wall system; (b) Band structure of the one-dimensional nanoribbon; (c) The modulus squared of wavefunction distribution of states A and B in each layer; (d) Top view of the structure and schematic of ZLMs and edge states; (e) and (f) The four-terminal conductance from lead R_1 to $L_{1,2,3}$ along the $-y$ direction and from lead L_1 to $R_{1,2,3}$ along the y direction, respectively; (g) and (h) Corresponding LDOS of (e) and (f), respectively.

with different magnetic domain walls, i.e., magnetic domain walls with purely out-of-plane magnetization in each domain, and different Néel domain walls. In Sec. IV, We give the thickness dependence of the electronic conductance for multilayer systems. Our summary is presented in Sec. V.

II. HAMILTONIAN AND CALCULATION METHODS

The low-energy electronic properties of MnBi$_2$Te$_4$ can be described by Bi-p_z and Te-p_z orbitals around Γ point [35], whereas Mn-d orbitals are farther away from the Fermi level. Based on the low-energy Hamiltonian of MnBi$_2$Te$_4$ [35–38], we construct the tight-binding model Hamiltonian [45–47] on the basis of $\{|p_{z,Bi}^+, \uparrow\rangle, |p_{z,Te}^-, \uparrow\rangle, |p_{z,Bi}^+, \downarrow\rangle, |p_{z,Te}^-, \downarrow\rangle\}$:

$$H = \sum_{\langle ij \rangle \alpha} c_i^\dagger T_\alpha c_j + \sum_i E_0 c_i^\dagger c_i + \sum_i (-1)^{n_z} m_0 c_i^\dagger c_i + \text{H.c.},$$

where $c_i^\dagger$ (c_i) is the creation (annihilation) operator of the electron at site i, $\langle \cdots \rangle$ denotes the nearest neighboring coupling, and $\alpha = x, y, z$. The first two terms represent the bulk Hamiltonian of topological insulator, with $T_\alpha = (B_\alpha \sigma_0 \otimes \tau_z + D_\alpha \sigma_0 \otimes \tau_0 - iA_\alpha \sigma_\alpha \otimes \tau_x)/2$ and $E_0 = (M_0 - \sum_\alpha B_\alpha)\sigma_0 \otimes \tau_z - \sum_\alpha D_\alpha \sigma_0 \otimes \tau_0$. The third term describes A-type antiferromagnetic interlayer coupling with $m_0 = m\sigma_z \otimes \tau_0$, where τ and σ are orbital and spin Pauli matrices, respectively. Various magnetic domain walls are reflected by the magnetization m. Other parameters are set to be $A_\alpha = A = 1.5$, $B_\alpha = B = 1.0$, $D_\alpha = D = 0.1$, and $M_0 = 0.3$ [47]; the magnetization strength is chosen to be $m = 0.35$.

The electronic transport properties are evaluated by the Landauer-Buttiker formula [48]:

$$G_{pq} = \frac{2e^2}{h} \text{Tr}[\Gamma_p G^r \Gamma_q G^a],$$

where $G^{r/a}$ are the retarded/advanced Green's functions of the central scattering region. $\Gamma_{p/q} = i[\Sigma_{p/q}^r - \Sigma_{p/q}^a]$ is the linewidth function describing the coupling between lead p/q and the central scattering region with self-energy $\Sigma^{r/a}$ of the leads. The local density of states (LDOS) injected from lead p is represented by $\rho_p(r, \varepsilon_F) = 1/2\pi [G^r \Gamma_p G^a]_{rr}$ [48], where the Fermi level is set to be $\varepsilon_F/B = 0.135$. When the Fermi level is in the bulk band gap, the LDOS is the same whether it is at the charge neutrality point or not (see Appendix B).

III. THE ELECTRONIC PROPERTIES OF ZLMS IN THREE-LAYER DOMAIN WALL SYSTEM

A. Domain wall with out-of-plane magnetization within each domain

We first construct a three-layer domain wall model with out-of-plane magnetization within each domain [see Fig. 1(a)]. The magnetic moments are represented by yellow and pink arrows in each layer. In our system, the y direction is infinite, whereas the x and z directions are finite. Due to the quantum anomalous Hall nature of intrinsic A-type antiferromagnetic topological insulators, the left and right sides of the domain wall have different topologies with opposite Chern numbers $\mathcal{C}$ [49], i.e., $\mathcal{C} = 1/-1$ for the left/right side.

Figure 1(b) displays the one-dimensional band structure, where the bulk bands, doubly-degenerate ZLMs (A) and edge states (B) are respectively denoted in black, orange and blue. The modulus squared of wavefunction distributions of states A and B are different, i.e., as shown in Fig. 1(c), the A states are dominantly distributed in the domain wall (middle) region, whereas the B states are mainly distributed at the boundaries. We can also find that both ZLMs and edge states are
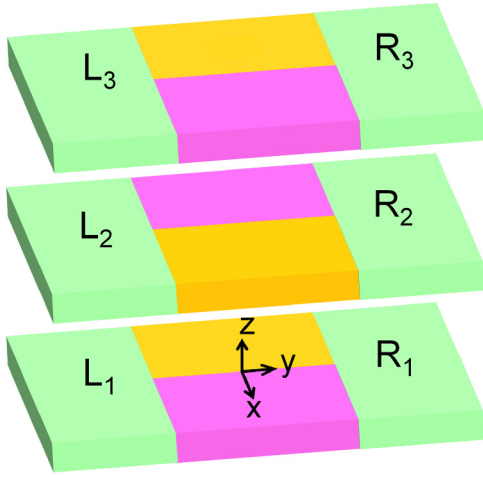
FIG. 2. The schematic diagram of leads connection in three-layer systems. The green ones are leads attached to each layer parallel to the y direction. The yellow and pink regions represent the different magnetic domains that make up the central scattering region, with the domain walls parallel to the y direction.

mainly located at the bottom and top layers with the same chirality of magnetization. These states are suppressed with backscattering and robust against weak disorders due to the spatially separated counter-propagation channels localized at interfaces and boundaries, respectively [9]. The left(right) side of the sample possesses net upward(downward) magnetization as shown by the black dot(cross) in the circle in Fig. 1(d). The orange arrows in the middle indicate the ZLMs, whereas the blue ones at the boundaries are edge states. The propagation directions of ZLMs and edge states are opposite.

To study the electronic transport properties, we consider a four-terminal mesoscopic device, where the electron injecting from one layer transits through the three-layer device and then exits from three independent terminals connected respectively with the three layers. The schematic diagram of leads connection is shown in Fig. 2. Due to the presence of M_z symmetry, the bottom and top layers are equivalent. Therefore, we focus on two situations, i.e., the incident terminal is linked with the bottom and middle layers, respectively.

Figures 1(e)–1(h) display the four-terminal conductances as a function of Fermi energy and the corresponding LDOS. The subscript i of $L(R)$ represents that the lead is the ith layer at $L(R)$ side. $R_i L_j (L_j R_i)$ represents that the electronic transport is from lead $R_i(L_j)$ to $L_j(R_i)$ [see Fig. 2]. When the electron is injected from R_1 to $L_{1,2,3}$ [see Fig. 1(e)], the conductance $G_{R_1 L_1}$ and $G_{R_1 L_3}$ are quantized to e^2/h, whereas $G_{R_1 L_2}$ vanishes, and the total conductance is quantized to be $2\,e^2/h$ when the Fermi energy is within the bulk gap, indicating that the electron is equally distributed in the layers with the same magnetization direction via interlayer coupling. When the electron is injected from L_1 to $R_{1,2,3}$ [see Fig. 1(f)], the conductance is the same as that from R_1 to $L_{1,2,3}$, but the physical origins are different, i.e., the electrons from sides R to L are mainly distributed around the domain walls in the bottom and top layers [see Fig. 1(g)], while the electrons from sides L to R are mainly located at the boundaries in the odd-number layers [see Fig. 1(h)], indicating that $G_{R_1 L_{1,2,3}}$
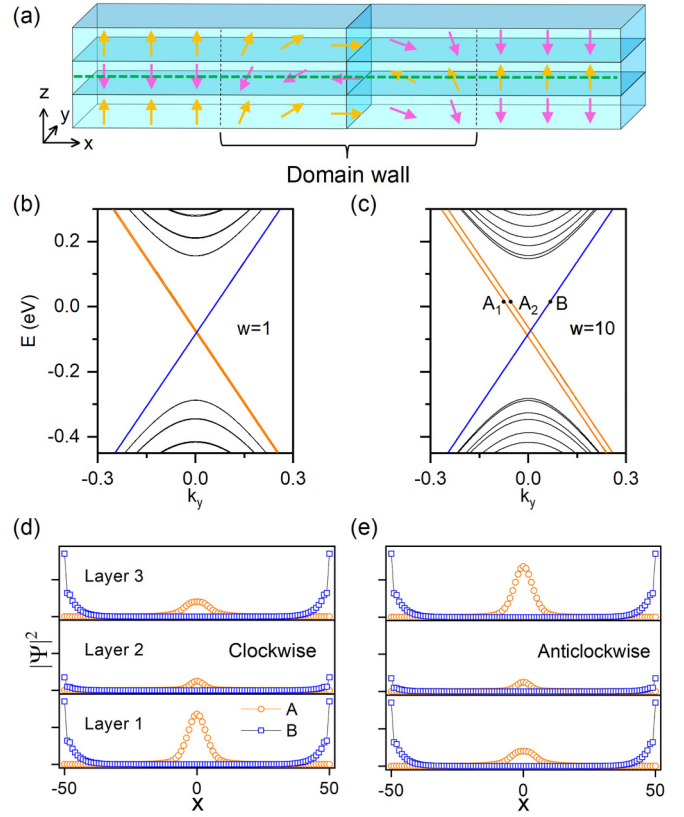

FIG. 3. (a) The three-layer systems with the Néel domain wall. The green dashed line in the middle layer is the mirror of clockwise configuration related to anticlockwise configuration; (b) and (c) Band structures with different domain wall widths represented by w; (d) and (e) The modulus squared of wavefunction distribution of A_1, A_2, and B states in every layer, respectively, where A is the total of A_1 and A_2.

and $G_{L_1 R_{1,2,3}}$ originate from the ZLMs and the edge states, respectively. When the electron is injected from the middle layer R_2 or L_2, the corresponding conductances of three independent outgoing terminals become vanishing, indicating the insulating nature of the middle layer.

B. The Néel domain wall

Besides above domain wall configuration with purely out-of-plane magnetization within each domain, the magnetic domain wall may be the Néel domain wall [50,51] as experimentally observed [32]. Here, the Néel domain wall is in the y direction with magnetization along x and z directions in Fig. 3(a). Two kinds configurations of the Néel domain wall are considered, i.e., clockwise configuration displayed in Fig. 3(a), and anticlockwise configuration related to clockwise configuration by M_z symmetry (the green dashed line in the middle layer is the mirror). Unlike the domain wall structure with purely out-of-plane magnetization within each domain, the Néel domain wall has finite domain wall width, which can further influence the electronic properties of ZLMs. Figures 3(b) and 3(c) plot the one-dimensional band structures with different domain wall widths. For a narrow domain wall width [Fig. 3(b)], the edge states (blue) keep degenerate whereas the ZLMs (orange) start to split in energy.

With the broadening of domain wall width [Fig. 3(c)], the energy splitting of ZLMs enlarges, whereas the edge states remain unchanged. Although the configurations of the Néel domain wall do not affect the band structures and edge states, they have influence on the modulus squared of wavefunction distributions of ZLMs. In the clockwise arrangement, as shown in Fig. 3(d), the ZLMs (labeled as *A*) are dominantly distributed in the domain wall (middle) region with a larger amplitude in the bottom layer; whereas in the anticlockwise configuration, as displayed in Fig. 3(e), the ZLMs are mainly distributed in the top layer of the domain wall region. These magnetic orientation-dependent topological conducting states can be used as current beam splitters in low-energy consumption electronics. The origin of the influence of the clockwise/anticlockwise configuration is explored in Appendix C.

To further explore the electronic transport properties, we consider three different situations, i.e., the current coming from the three independent layers, respectively. Although the top and bottom layers are nonequivalent due to the breaking of M_z symmetry, we find that the four-terminal conductances and the corresponding LDOS are the same for the current incoming from the top or bottom layer. For the current incoming from the middle layer, the conductances of three independent terminals are vanishing, indicating the insulating nature of the system. Hereinbelow, we focus on the system with the current incoming from the bottom layer.

Figure 4 displays the four-terminal conductances and corresponding LDOS with different Néel domain wall configurations. As aforementioned, the conductance from *R* to *L* side is originated from the ZLMs [see Figs. 4(a)–4(d)], whereas the conductance from *L* to *R* side comes from the edge states [see Figs. 4(e)–4(h)], with the total conductance being quantized to $2e^2/h$ for Fermi levels inside the bulk band gap.

For the clockwise magnetization [see Figs. 4(a) and 4(b)], $G_{R_1L_1} \approx 1.24\, e^2/h$ is about twice of $G_{R_1L_3}$, and $G_{R_1L_2} \approx 0.15\, e^2/h$. For the anticlockwise magnetization, as shown in Figs. 4(c) and 4(d), the conductances $G_{R_1L_3}$ and $G_{R_1L_1}$ are reversed, and $G_{R_1L_2} \approx 0.15\, e^2/h$ keeps unchanged for Fermi levels inside the bulk band gap. In contrast, the edge states induced conductance $G_{L_1R_1}$ and $G_{L_1R_3}$ are quantized to be $1.0\, e^2/h$, whereas $G_{L_1R_2}$ is vanishing, which are independent of the magnetization configurations [see Figs. 4(e) and 4(g)]. One can also observe that the edge states are distributed at the boundaries of the top and bottom layers from the LDOS [see Figs. 4(f) and 4(h)]. The different distributions of ZLMs at the bottom and top layers can be attributed to the M_z symmetry breaking from the in-plane magnetization components. In fact, the bottom (top) layer of the clockwise configuration is related to the top (bottom) layer of the anticlockwise configuration by M_z symmetry. The above results indicate that the conductance and LDOS distributions can be easily tuned by the Néel domain wall configurations and the direction of incident lead.

We also explore the electronic properties of a five-layer system [see Appendix E]. Similar to the results of the three-layer system, we find that the total conductance for Fermi levels inside the bulk gap is always quantized to $2.0\, e^2/h$, regardless of the number of layers. In the presence of only out-of-plane magnetization, the ZLMs are still only distributed in the odd-number layers, with a larger distribution in the outer-
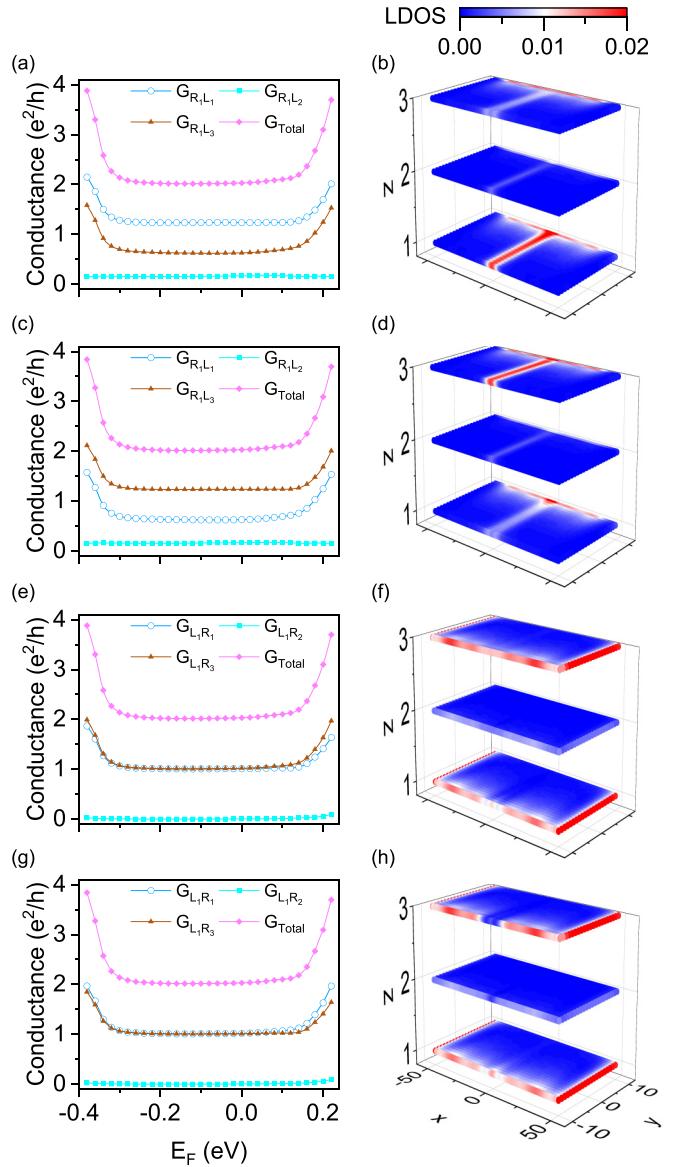

FIG. 4. The four-terminal conductances and corresponding LDOS of three-layer systems with the Néel domain wall. (a)–(d) From lead R_1 to $L_{1,2,3}$ along $-y$ direction, where (a) and (b) are for the clockwise configuration and (c) and (d) are for the anticlockwise configuration; (e)–(h) From lead L_1 to $R_{1,2,3}$ along y direction, where (e) and (f) are for the clockwise configuration and (g) and (h) are for the anticlockwise configuration.

most layers, whereas the edge states are also distributed in the odd-number layers with equal amplitude. In the presence of the Néel domain wall, although the distribution of edge states is unchanged, the distribution of ZLMs can be effectively tuned by the clockwise/anticlockwise magnetization.

IV. THICKNESS DEPENDENCE OF CONDUCTANCE IN MULTILAYER DOMAIN WALL SYSTEM

The above electronic transport characteristics are also applicable to thicker samples with antiferromagnetic domain walls. To quantitatively investigate the thickness dependence of electronic distribution in multilayers, we calculate the
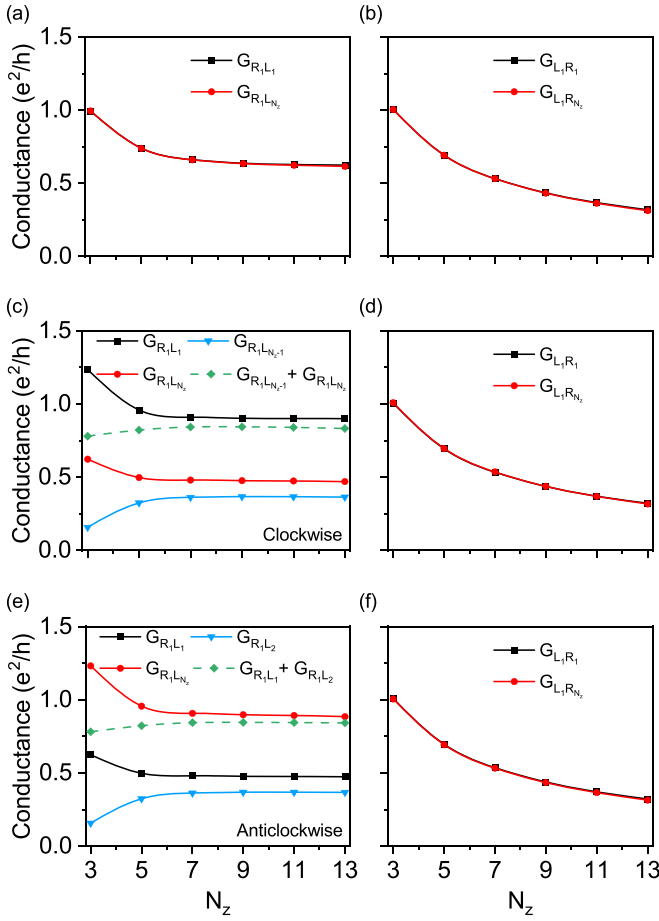
FIG. 5. Thickness dependence of conductance in multilayer domain wall system. (a) and (b) For the system with purely out-of-plane magnetization; (c) and (d) For the system with the Néel domain wall of clockwise configuration; (e) and (f) For the system with the Néel domain wall of anticlockwise configuration. The conductance in the left column is contributed from ZLMs, whereas that in right column originates from the edge states.

electronic transport properties of the multi-terminal system connected separately with each lead, i.e., the input lead is only connected with the bottom layer whereas the output leads connect separately with each layer of the system.

Figures 5(a) and 5(b) display the conductances as a function of the number of layers N_z with only the out-of-plane magnetization. Because the modulus squared of wavefunction is mainly distributed at the outermost layers for purely out-of-plane magnetization system, we focus on the conductance of the corresponding layers, $G_{R_1 L_1}$ and $G_{R_1 L_{N_z}}$. As shown in Fig. 5(a), the conductances $G_{R_1 L_1}$ and $G_{R_1 L_{N_z}}$ from ZLMs are equal, and gradually decay from 1.0 e^2/h for $N_z = 3$ to 0.66 e^2/h for $N_z = 7$, then decrease slowly when $N_z > 7$, indicating that the conductance leaving from the outermost layers are gradually saturated with the increase of the layer numbers. It is noteworthy that the total conductance is quantized to 2.0 e^2/h for Fermi energies inside the bulk band gap, implying that $G_{R_1 L_1}$ and $G_{R_1 L_{N_z}}$ are still dominant for the electronic transport properties. Since the edge states are distributed in the odd-number layers with equal amplitude, the conductance

$G_{L_1 R_1}$ and $G_{L_1 R_{N_z}}$ from quantum anomalous Hall edge states gradually decrease to $\frac{2}{n} e^2/h$ ($N_z = 2n - 1$) with the increase of thickness, where n denotes the number of odd-number layers [see Fig. 5(b)]. The conductance from edge states as a function of thickness is the same for the domain wall with purely out-of-plane within each domain and the Néel domain wall [see the right column of Fig. 5].

In the presence of clockwise Néel domain wall, as displayed in Fig. 5(c), $G_{R_1 L_1}$ and $G_{R_1 L_{N_z}}$ from ZLMs are different, i.e., $G_{R_1 L_1} > G_{R_1 L_{N_z}}$. However, their variations are similar, i.e., they gradually decrease from $N_z = 3$ to $N_z = 7$, then become almost unchanged for $N_z > 7$. The presence of the in-plane magnetization components leads to the existence of the states in the even-number layers (e.g., $N_z - 1$), indicating a conducting channel (nonzero conductance of $G_{R_1 L_{N_z-1}}$). We can find that $G_{R_1 L_{N_z-1}}$ gradually increases as a function of layer thickness with a saturated value of 0.36 e^2/h. The sum of $G_{R_1 L_{N_z}}$ and $G_{R_1 L_{N_z-1}}$ are about 0.84 e^2/h and are comparable with $G_{R_1 L_1}$ [see the green dashed line in Fig. 5(c)], which implies that the three conductances dominate the electronic transport properties. In the presence of anticlockwise configuration, the results are similar to that of clockwise configuration, but with a relation of $G_{R_1 L_{N_z}} > G_{R_1 L_1} > G_{R_1 L_2}$.

V. SUMMARY

In conclusion, we theoretically propose a feasible scheme to achieve intrinsic topologically protected conducting channels, i.e., the ZLMs in the antiferromagnetic topological insulator $MnBi_2Te_4$ odd-number layer systems with different types of magnetic domain walls, and the distributions of these channels are layer-dependent and can be tuned by magnetic domain wall configurations and the choice of the injected leads. We can use these electronic transport results to predict or distinguish the internal magnetic domain wall structures. Our study can shed light on designing low-power topological quantum devices and beam splitters, and has broad application prospects in magnetic memory and spintronic devices [52]. Our results are not only applicable to the $MnBi_2Te_4$ system. When the system is a layered interlayer antiferromagnetic topological insulator with domain walls, the similar layer-dependent electronic transport properties can be obtained.

APPENDIX A: THE TWO-DIMENSIONAL AND ONE-DIMENSIONAL HAMILTONIAN

We give the three-dimensional model Hamiltonian in the main text. We calculate the Chern number in the two-dimensional system which has translational symmetry along x

and y directions and the corresponding momenta k_x and k_y are good quantum numbers. The two-dimensional Hamiltonian in reciprocal space is

$$H_{2D}(\boldsymbol{k}) = \sum_{\boldsymbol{k},z} c_{\boldsymbol{k}}^{\dagger}(z)[E_0 + (-1)^{n_z} m_0] c_{\boldsymbol{k}}(z)$$
$$+ \left[\sum_{\boldsymbol{k},z} c_{\boldsymbol{k}}^{\dagger}(z) \left(T_x e^{ik_x} + T_y e^{ik_y} \right) c_{\boldsymbol{k}}(z) \right.$$
$$\left. + c_{\boldsymbol{k}}^{\dagger}(z+1) T_z c_{\boldsymbol{k}}(z) + \text{H.c.} \right], \tag{A1}$$

where $\boldsymbol{k} = (k_x, k_y)$. In a one-dimensional system, there is translational symmetry only along the y direction, so only k_y is a good quantum number. It is finite-size along the x and z directions. The one-dimensional Hamiltonian is

$$H_{1D}(k_y) = \sum_{k_y,x,z} c_{k_y}^{\dagger}(x,z)[E_0 + (-1)^{n_z} m_0] c_{k_y}(x,z)$$
$$+ \left[\sum_{k_y,x,z} c_{k_y}^{\dagger}(x,z) T_y e^{ik_y} c_{k_y}(x,z) \right.$$
$$+ c_{k_y}^{\dagger}(x, z+1) T_z c_{k_y}(x,z)$$
$$\left. + c_{k_y}^{\dagger}(x+1, z) T_x c_{k_y}(x,z) + \text{H.c.} \right]. \tag{A2}$$

APPENDIX B: THE LDOS AT THE CHARGE NEUTRALITY POINT

From the band structure in the main text, we know that the range of bulk band gap is approximately from -0.25 to 0.15, so in the main text we take the Fermi level $\varepsilon_F/B = 0.135$ which is in the bulk band gap. The distribution of electronic states remains unchanged inside the bulk gap regardless of the position of the Fermi level. To clearly demonstrate this, we calculate the LDOS at the charge neutrality point (about -0.0781) [see Fig. 6]. One can observe that the distributions of both the ZLMs and edge states are consistent with the previous results for the Fermi level at 0.135.

APPENDIX C: THE INFLUENCE OF THE NÉEL DOMAIN WALL ON THE DISTRIBUTION OF WAVEFUNCTIONS IN DIFFERENT LAYERS

In the previous results, we see that for the clockwise/anticlockwise Néel domain wall system, the ZLMs are mainly distributed in the bottom/top layer. We now explore its mechanism. We know from the front that there are almost no states in the second layer in three-layer systems. We therefore consider three cases, i.e., (i) only the first layer, (ii) only the third layer, and (iii) both the first and third layers have the clockwise Néel domain wall, as shown in Fig. 7.

In the three cases, the band structures are almost the same and the edge states are equally distributed in the first and third layers. However, the electronic distributions of ZLMs are different. Compared with the purely out-of-plane magnetization system in which ZLMs are equally distributed in layer one and layer three, when only the first layer has the clockwise
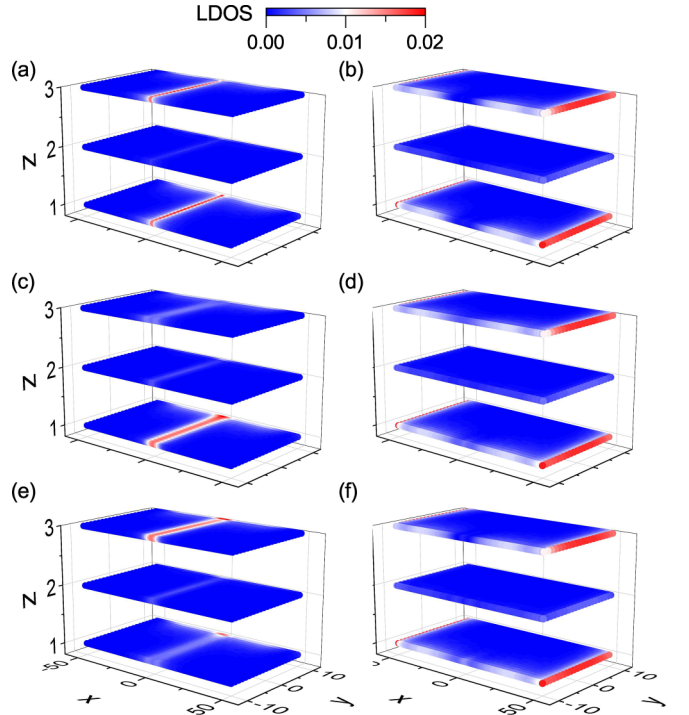

FIG. 6. The LDOS with different magnetic domain-wall configurations of the three-layer systems. (a) and (b) For the system with purely out-of-plane magnetization; (c) and (d) For the system with the clockwise Néel domain wall; (e) and (f) For the system with the anticlockwise Néel domain wall. The LDOS in the left column is contributed from ZLMs whereas that in right column originates from the edge states.

Néel domain wall as displayed in Fig. 7(a), the distributions of ZLMs in layer one are larger than that in layer three, indicating that the clockwise Néel domain wall in layer one enhances the distribution of ZLMs in layer one. When only the third layer has the clockwise Néel domain wall, as displayed in Fig. 7(b), the distribution of ZLMs in the third layer is reduced and smaller than that in the first layer. When both the first and third layers have the clockwise Néel domain wall, as shown in Fig. 7(c), the ZLMs of the first layer are enhanced and the ZLMs of the third layer is weakened, resulting in a larger distribution of ZLMs in the first layer than that in the third layer. When the second layer has the clockwise Néel domain wall, it has no qualitative effect on the final results. Furthermore, when all three layers have the Néel domain wall, we can naturally obtain the results that the ZLMs are mainly distributed in layer one.

Similarly, we construct three anticlockwise Néel domain wall systems, as shown in Fig. 8. The anticlockwise Néel domain wall in the first layer can decrease the distribution of ZLMs in layer one [see Fig. 8(a)], while it in the third layer can increase the ZLMs in layer three [Fig. 8(b)]. When both the first and third layers have the anticlockwise Néel domain wall, the distribution of ZLMs in layer three is larger than that in layer one [Fig. 8(c)]. When the second layer has the anticlockwise Néel domain wall, it has no qualitative effect on the final results. Therefore, when all three layers have anticlockwise Néel domain wall, the result is that the ZLMs mainly distribute in layer three.
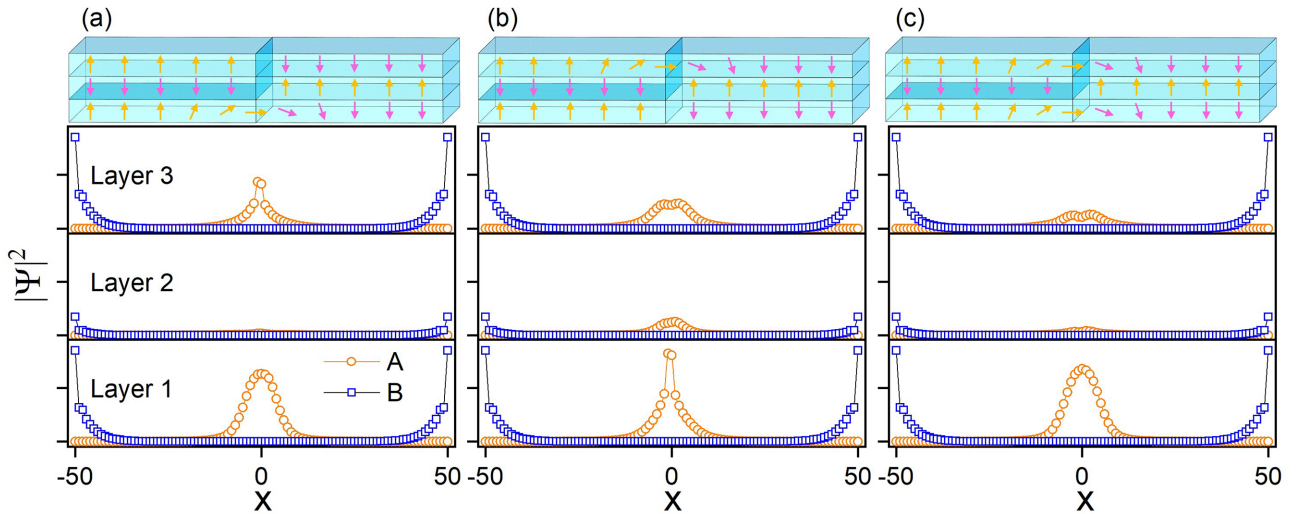
FIG. 7. The upper row represents the different magnetization configurations in which some layers have the clockwise Néel domain wall. The bottom row is the modulus squared of wavefunction distribution of A and B states in every layer, where A is the ZLMs and B is the edge states.

APPENDIX D: THE TWO-TERMINAL ELECTRONIC TRANSPORT PROPERTIES IN THREE-LAYER DOMAIN WALL SYSTEM

When the leads and the central scattering region are perfectly matched, i.e., they have the same width along x direction and number of layers along z direction. In three-layer system, the injected terminal has three layers attached to the scattering region at $R(L)$ side and the outgoing terminal also has three layers at $L(R)$ side. When the system has purely out-of-plane magnetization in each domain, as shown in Figs. 9(a) and 9(c), the conductance is quantized to $2\,e^2/h$ when the Fermi energy is located inside the bulk band gap. Although the two-terminal conductance G_{RL} and G_{LR} are the same, the origins are different, i.e., the electrons from the R side to the L side are mainly distributed around the domain walls in the bottom and top layers [see Fig. 9(b)], while the electrons from the L side to the R side are mainly located at the boundaries in the bottom and top layers [see Fig. 9(d)], indicating that G_{RL} and G_{LR} originate from the ZLMs and the edge states, respectively. The above two-terminal electronic transport properties are consistent with the band structures and modulus squared of wavefunction distributions in Fig. 1 of the main text.

Similar to the results of the system with purely out-of-plane magnetization, the system with the Néel domain wall has the same two-terminal conductance G_{RL} and G_{LR} [see Figs. 10(a) and 10(b)] which have different origins, i.e., the electrons from the R side to the L side are originated from ZLMs and are mainly distributed around the domain walls [see Figs. 10(c) and 10(e)], while the electrons from the L side to the R side are mainly located equally at the boundaries in the bottom and top layers [see Figs. 10(d) and 10(f)]. The influence of
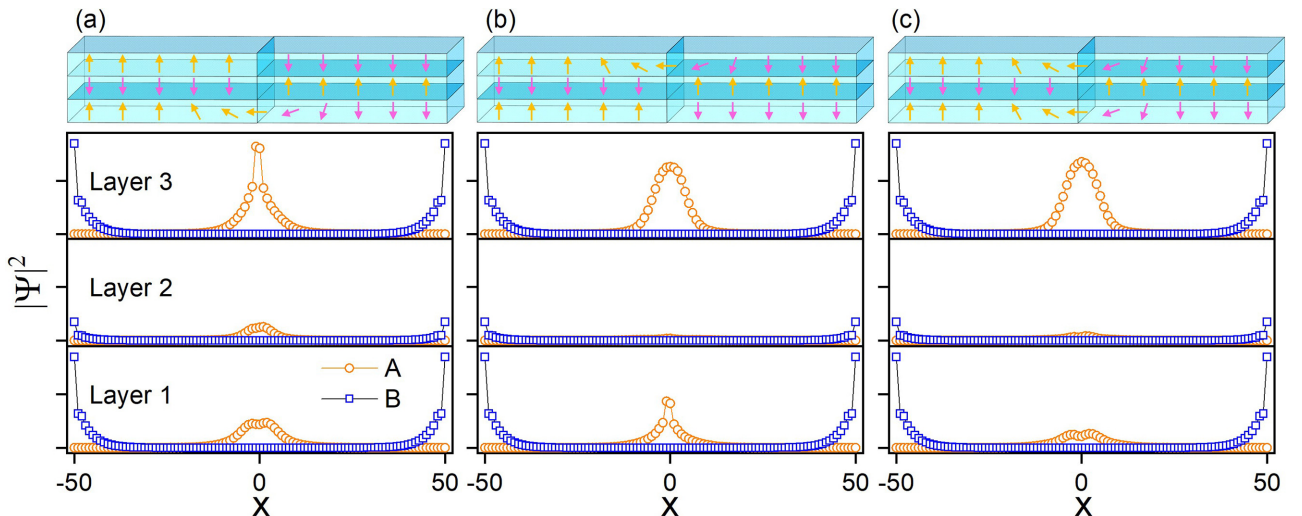

FIG. 8. The upper row represents the different magnetization configurations in which some layers have the anticlockwise Néel domain wall. The bottom row is the modulus squared of wavefunction distribution of A and B states in every layer, where A is the ZLMs and B is the edge states.
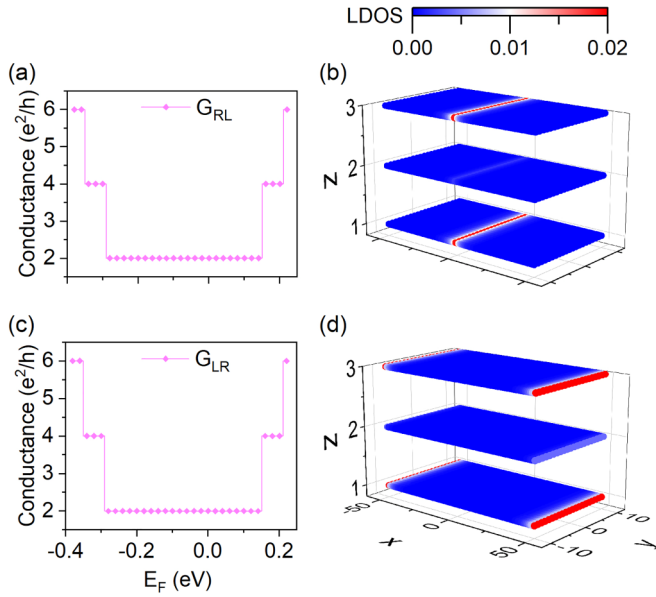
FIG. 9. The two-terminal conductance and corresponding LDOS with purely out-of-plane magnetization in three-layer system. (a) and (b) From lead R to L along $-y$ direction. (c) and (d) From lead L to R along y direction.
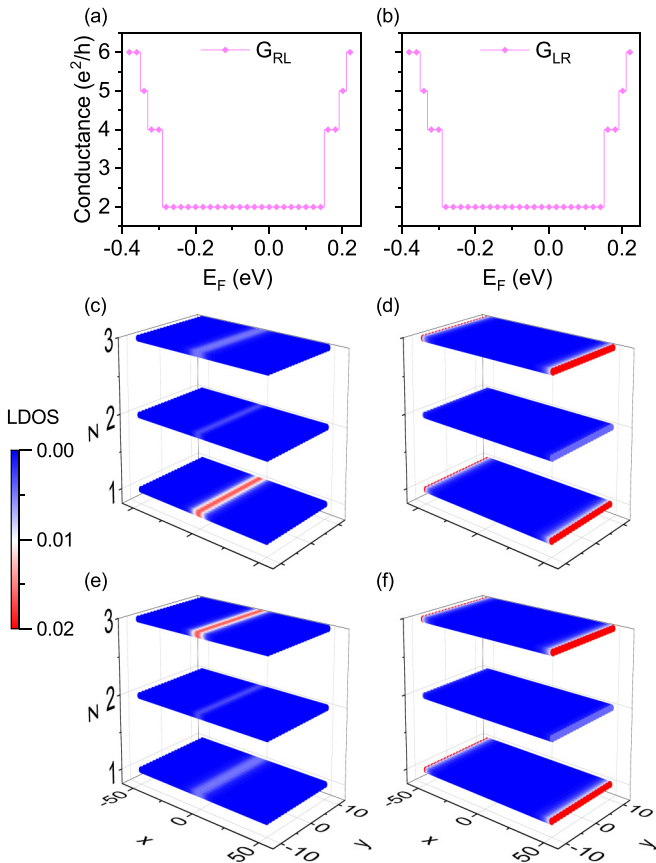

FIG. 10. The two-terminal conductance and corresponding LDOS with the Néel domain wall in three-layer system. The left column is from lead R to L along $-y$ direction, whereas the right column is from lead L to R along y direction, where (c) and (d) are LDOS for the clockwise configuration and (e) and (f) are LDOS for the anticlockwise configuration.

the Néel domain wall configurations on the distributions of ZLMs can be clearly observed in Figs. 10(c) and 10(e), i.e., the ZLMs are dominantly distributed in the bottom/top layer for clockwise/anticlockwise magnetization system. However, the changes of magnetization configurations do not affect the distribution of edge states as demonstrated in Figs. 10(d) and 10(f).

APPENDIX E: THE ELECTRONIC PROPERTIES OF ZLMS IN FIVE-LAYER DOMAIN WALL SYSTEM

1. Domain wall with out-of-plane magnetization within each domain

A five-layer domain wall model with purely out-of-plane magnetization within each domain is displayed in Fig. 11(a). The left and right sides of the domain wall have opposite Chern number $\mathcal{C}$, i.e., $\mathcal{C} = 1$ for left side and $\mathcal{C} = -1$ for the right side. The one-dimensional band structure of the system is displayed in Fig. 11(b), where the bulk states, doubly-degenerated ZLMs (A) and edge states (B) are denoted by black, orange and blue, respectively. The modulus squared of wavefunction distributions of A and B are different, i.e., as shown in Fig. 11(c), the A states are dominantly distributed in the domain wall (middle) region, whereas the B states are mainly distributed at the boundaries. We can also find that both ZLMs and edge states are mainly located at the odd-number layers with the same chirality of magnetization. The propagation directions of ZLMs and edges states are opposite, as displayed in Fig. 11(d). These characteristics are the same as that in the three-layer system with purely out-of-plane magnetization.

As can be seen from Fig. 11(c), the ZLMs dominantly distribute in the outermost layers (i.e., the bottom and top layers), while the edge states distribute in the odd number layers equally. Now we explore the factors that influence this distribution. When the interlayer coupling is doubled, as shown in Fig. 12(a), both the ZLMs and edge states are mainly distributed in the outermost layers, i.e., the electronic distributions of ZLMs and edge states in the bottom and top layers are larger than that in the third layer. When the interlayer coupling is reduced to half of the original value, as shown in Fig. 12(b), the ZLMs are mainly distributed in the outermost layers, and the edge states are equally distributed in the odd layers. The above results clearly show the crucial role of interlayer coupling in determining the electronic distributions of ZLMs and edge states in different layers. And regardless of increasing or decreasing the interlayer coupling strength, the ZLMs mainly distribute in the outermost layers. The interlayer coupling strength can be used to tune the distribution of states in different layers.

We study the two-terminal electronic transport properties of the five-layer system with purely out-of-plane magnetization in each domain. The schematic diagram of leads connection is shown in Fig 13. When the leads and the central scattering region are perfectly matched, as shown in Figs. 14(a) and 14(c), the conductance is quantized with a value of $2\,e^2/h$ when the Fermi energy is located inside the bulk band gap. Although the two-terminal conductance G_{RL} and G_{LR} are the same, the origins are different, i.e.,
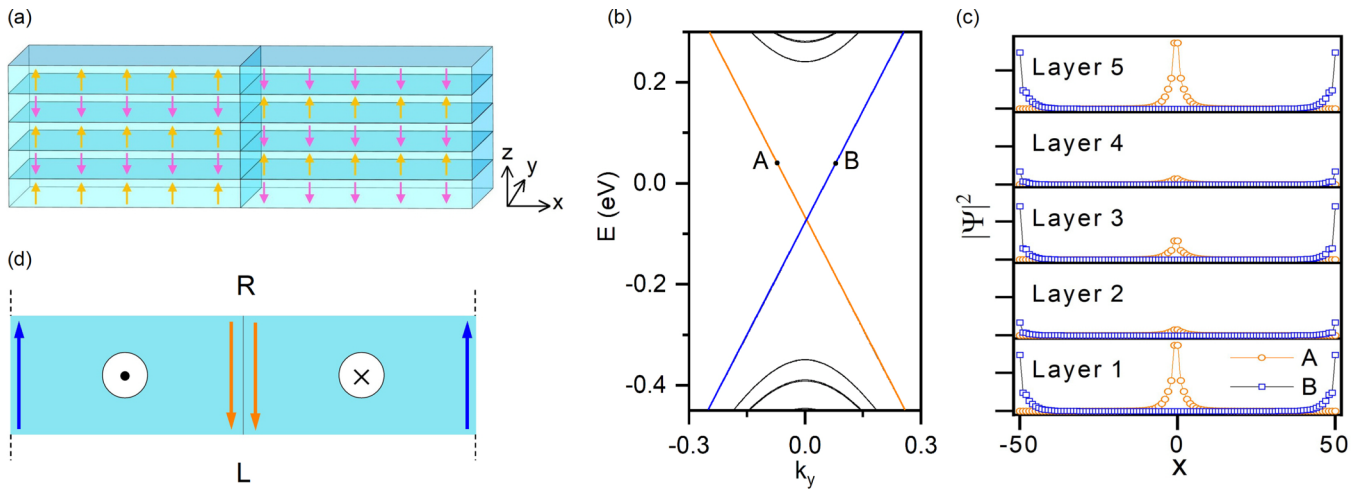
FIG. 11. (a) Front view of the five-layer system with purely out-of-plane magnetization within each domain; (b) Band structure of the one-dimensional nanoribbon; (c) The modulus squared of wavefunction distributions for states A and B in every layer; (d) Top view of the structures and schematic of ZLMs and edge states.

the electrons from the R side to the L side are mainly distributed around the domain walls in the odd-number layers [see Fig. 14(b)], while the electrons from the L side to the R side are mainly located at the boundaries in the odd-number layers [see Fig. 14(d)], indicating that G_{RL} and G_{LR} originate from the ZLMs and the edge states, respectively. The above two-terminal electronic transport properties are consistent with the band structure and modulus squared of wavefunction distributions in Fig. 11.

To further explore electronic properties in this system, we consider a six-terminal transport device, where the electron injecting from one layer transits through the five-layer device and then exits from five independent terminals connected respectively with the five layers of the central device. Due to the presence of M_z symmetry, the bottom and top layers are equivalent, and the second and fourth layers are equivalent, respectively. Hence, we consider three cases, i.e., the metallic

incident lead is from the bottom layer, the second layer, and the third layer, respectively.

Figure 15 displays the six-terminal conductance as a function of Fermi energy and the corresponding LDOS. When the electron is injected from R_1 to $L_{1,2,3,4,5}$ [see Fig. 15(a)], the conductance $G_{R_1L_1} = G_{R_1L_5} > G_{R_1L_3}$, whereas $G_{R_1L_2}$ and
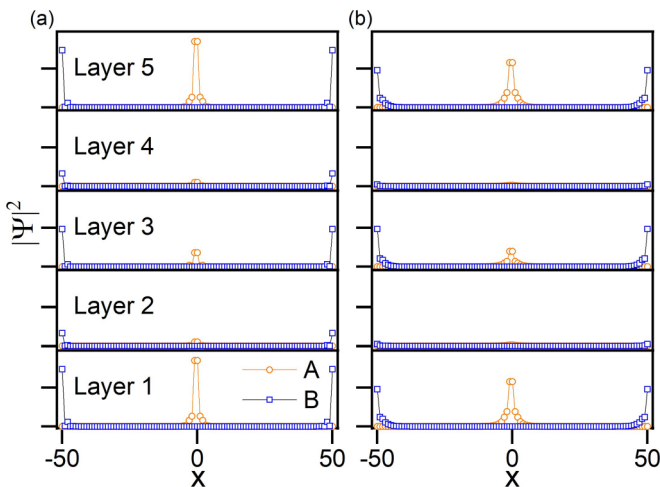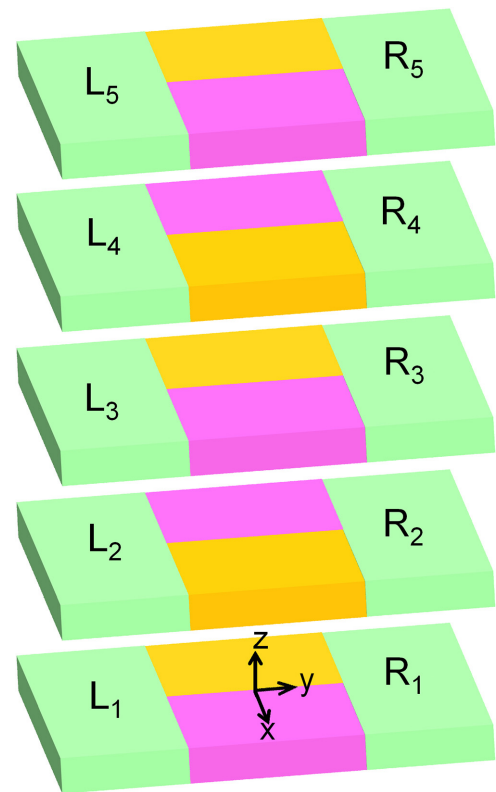

FIG. 13. The schematic diagram of leads connection in five-layer systems. The green ones are leads attached to each layer parallel to the y direction. The yellow and pink regions represent the different magnetic domains that make up the central scattering region, with the domain walls parallel to the y direction.

FIG. 12. The effect of interlayer coupling on the distribution of wavefunction in five-layer system with purely out-of-plane magnetization, where A represents ZLMs and B represents edge states. (a) Double interlayer coupling; (b) Half interlayer coupling.
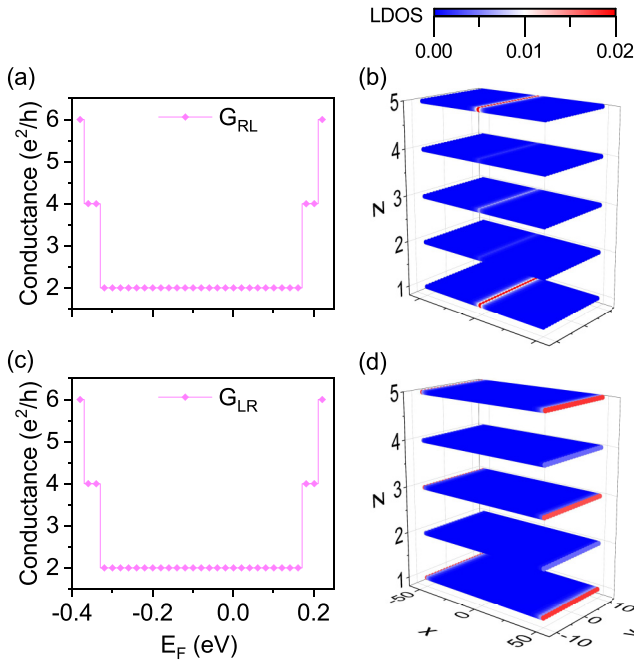
FIG. 14. The two-terminal conductance and corresponding LDOS of the five-layer system with purely out-of-plane magnetization. (a) and (b) From lead R to L along $-y$ direction; (c) and (d) From lead L to R along y direction.

$G_{R_1L_4}$ are vanished inside the bulk band gap, indicating that the electron is distributed in the layers with the same magnetization configuration via interlayer coupling. And the total conductance from R_1 to $L_{1,2,3,4,5}$ is quantized to $2\,e^2/h$ when
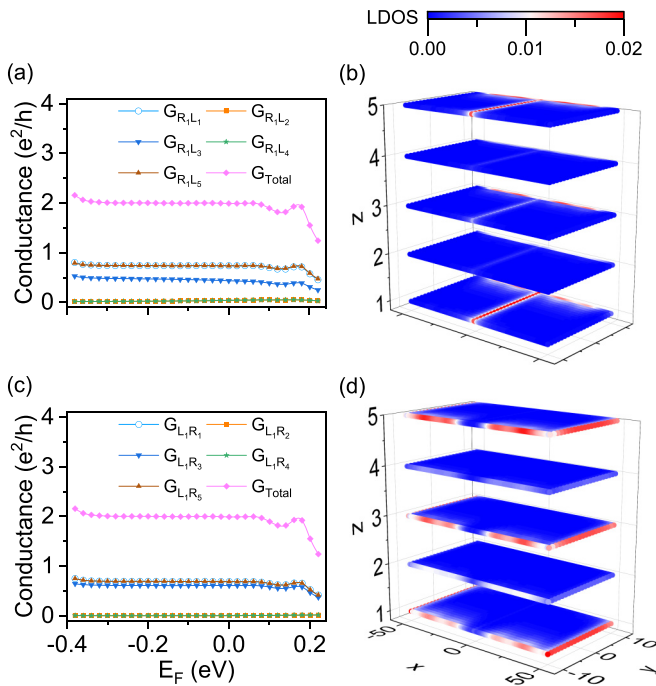

FIG. 15. The six-terminal conductance and corresponding LDOS of the five-layer system with purely out-of-plane magnetization. (a) and (b) From lead R_1 to $L_{1,2,3,4,5}$ along $-y$ direction. (c) and (d) From lead L_1 to $R_{1,2,3,4,5}$ along y direction.
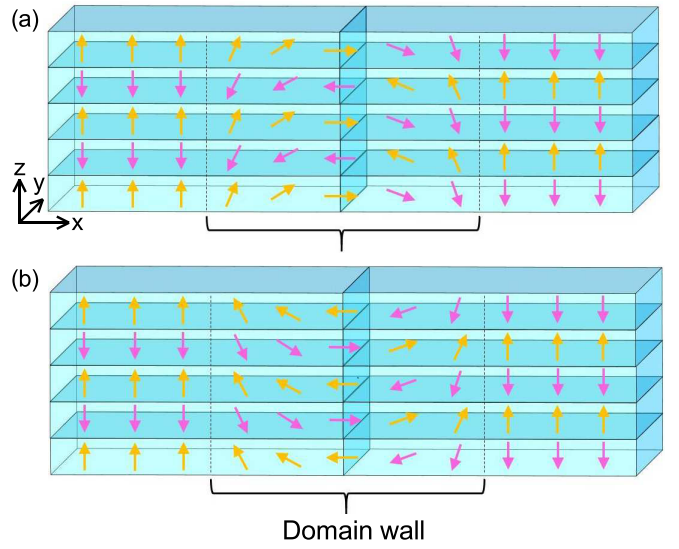

FIG. 16. The five-layer system with the Néel domain wall. The magnetic domain wall configuration is: (a) clockwise; (b) anticlockwise.

the Fermi energy is located inside the bulk band gap. The corresponding LDOS explicitly demonstrates that the states are dominantly distributed in the bottom and top layers and part of them are on the third layer [see Fig. 15(b)]. When the
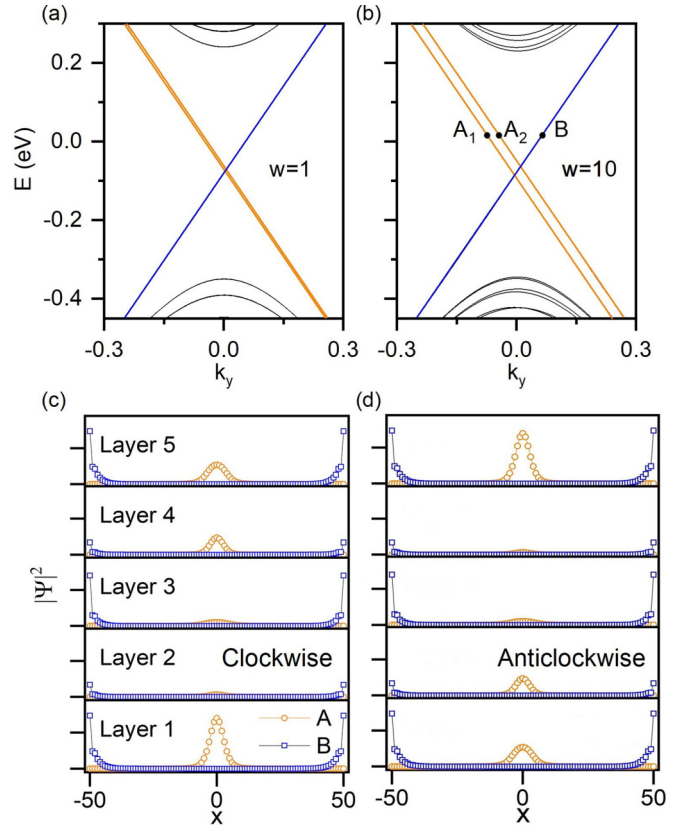

FIG. 17. (a) and (b) Band structures of the five-layer Néel domain wall systems with different domain wall widths represented by w. (c) and (d) The distribution of wave functions for clockwise/anticlockwise configuration respectively of A_1, A_2, and B labeled in (b), where A is the total of A_1 and A_2.
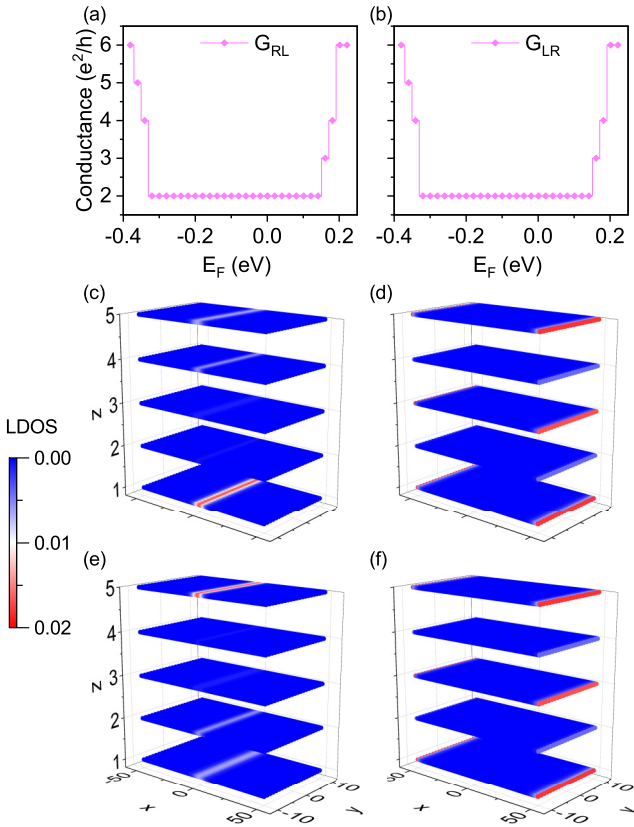
FIG. 18. (a) and (b) The two-terminal conductance of the five-layer system with the Néel domain wall. The left column is contributed from ZLMs whereas that the right column originates from the edge states. (c) and (d) The corresponding LDOS of the clockwise configuration. (e) and (f) The corresponding LDOS of the anticlockwise configuration.

electron is injected from L_1 to $R_{1,2,3,4,5}$ [see Fig. 15(c)], the conductance $G_{R_1L_2} = G_{R_1L_4} = 0$ are the same as that from R_1 to $L_{1,2,3,4,5}$, whereas the conductance $G_{L_1R_1} = G_{L_1R_3} = G_{L_1R_5}$ is different from that from R_1 to $L_{1,2,3,4,5}$, and the corresponding LDOS shows that the states are distributed at the boundaries of the odd-number layers equally [see Fig. 15(d)]. Although the electronic distributions in Figs. 14 and 15 are similar, the different incident lead configurations reveal the interchannel coupling induced electronic interference in the five-layer system. When the electron is injected from the third or the top layer, the results are the same as that from the bottom layer. When the electron is injected from the second or the fourth layer, the corresponding conductance of five independent output terminals are vanished, indicating the insulating nature of the even-number layers.

2. The Néel domain wall

In a five-layer domain wall configuration, the Néel domain wall configurations are displayed in Figs. 16(a) and 16(b), where two types of configurations (clockwise/anticlockwise) are considered. The magnetization direction gradually flips in the domain wall region of each layer.

Figures 17(a) and 17(b) plot the one-dimensional band structures with different domain wall widths. For a short
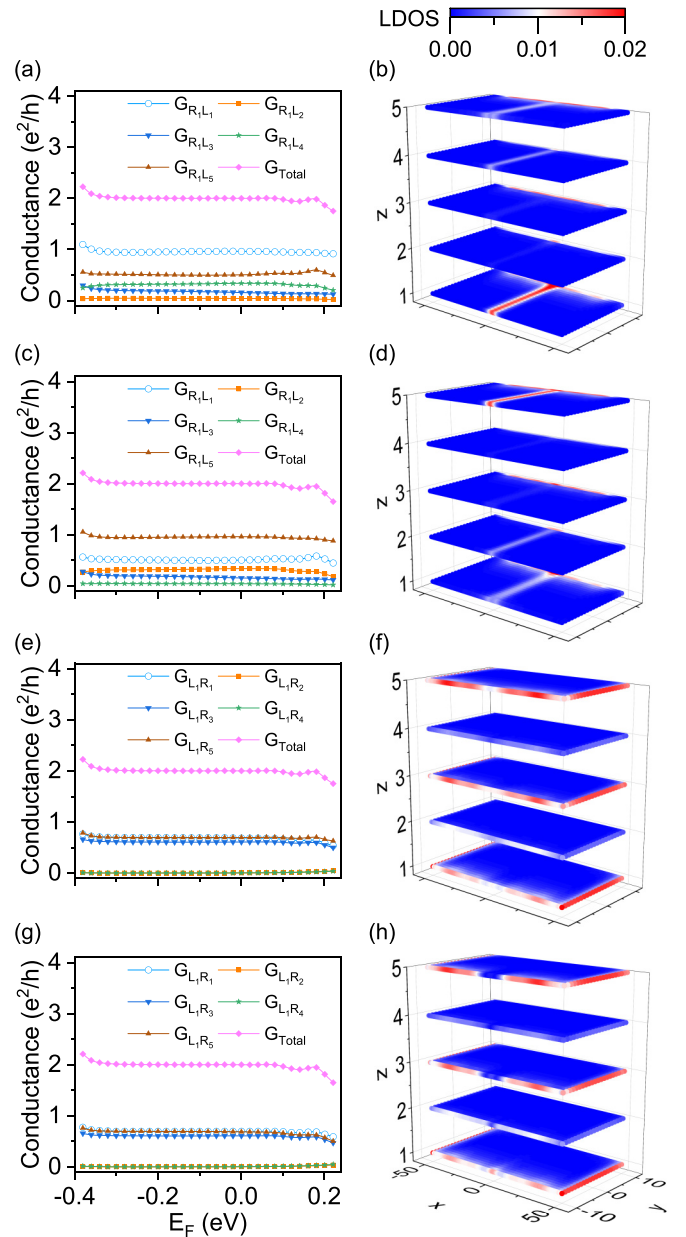

FIG. 19. The six-terminal conductance and corresponding LDOS of the five-layer system with the Néel domain wall. (a)–(d) From lead R_1 to $L_{1,2,3,4,5}$ along $-y$ direction, where (a) and (b) are for the clockwise configuration and (c) and (d) for the anticlockwise configuration. (e)–(h) From lead L_1 to $R_{1,2,3,4,5}$ along y direction, where (e) and (f) are for the clockwise configuration and (g) and (h) for the anticlockwise configuration.

domain wall width [Fig. 17(a)], the edge states (blue) keep degenerate whereas the ZLMs (orange) start to split in energy. With the increase of domain wall width [Fig. 17(b)], the energy splitting of ZLMs enlarges whereas the edge states remain unchanged.

Although the configurations of the Néel domain wall do not affect the band structures and edge states, they have an influence on the ZLMs. In the clockwise arrangement, as shown in Fig. 17(c), the ZLMs (labeled as A) are dominantly distributed in the domain wall (middle) region with a larger

amplitude in the bottom layer; whereas in the anticlockwise configuration, as displayed in Fig. 17(d), the ZLMs are mainly distributed in the top layer of the domain wall region.

The above characteristics of band structures and modulus squared of wavefunction distributions can be further understood by the electronic transport calculations as shown in Fig. 18. Similar to the results of the system with purely out-of-plane magnetization, the same two-terminal conductance G_{RL} and G_{LR} [see Figs. 18(a) and 18(b)] have different origins, i.e., the electrons from the R side to the L side are originated from ZLMs and are mainly distributed around the domain walls [see Figs. 18(c) and 18(e)], while the electrons from the L side to the R side are mainly located equally at the boundaries in the odd-number layers [see Figs. 18(d) and 18(f)]. The influence of the Néel domain wall configurations on the distributions of ZLMs can be clearly observed in Figs. 18(c) and 18(e), i.e., the electrons dominantly transmit through the bottom/top layer for clockwise/anticlockwise magnetization. However, the changes of magnetization directions do not affect the distribution of edge states as demonstrated in Figs. 18(d) and 18(f).

To further explore the electronic properties in this system, we consider a six-terminal transport device. We consider five cases, i.e., the metallic incident lead is from (i) the bottom layer, (ii) the second layer, (iii) the third layer, (iv) the fourth layer, and (v) the top layer, respectively. Although the bottom, third and top layers are not equivalent due to the breaking of

M_z symmetry, we find that the six-terminal conductance and the corresponding LDOS are the same for the incident lead from the bottom/third/top layer. For the incident lead from the second/fourth layer, the conductance of five independent output terminals are vanished, indicating the insulating nature of the system. Therefore, hereinbelow we focus on the case of incident lead from the bottom layer.

Figure 19 displays the six-terminal conductance and the corresponding LDOS with different Néel domain wall configurations. As aforementioned, the conductance from the R side to the L side is originated from the ZLMs [see Figs. 19(a)–19(d)], whereas the conductance from the L side to the R side comes from the edge states [see Figs. 19(e)–19(h)], with the total conductance quantized to $2\,e^2/h$ inside the bulk band gap. For clockwise magnetization, as shown in Figs. 19(a) and 19(b), the conductance $G_{R_1L_1} \approx 0.96\,e^2/h$ is about twice that of $G_{R_1L_5}$, and a small $G_{R_1L_4} \approx 0.32\,e^2/h$ still exists. For anticlockwise magnetization, as shown in Figs. 19(c) and 19(d), the conductance $G_{R_1L_1}$ and $G_{R_1L_5}$ are reversed, and $G_{R_1L_2} \approx 0.32\,e^2/h$ replaces $G_{R_1L_4}$ inside the bulk band gap. Contrastingly, when the electron is injected from L_1 to $R_{1,2,3,4,5}$, the edge states induced conductance $G_{L_1R_1} = G_{L_1R_5} \approx 0.70\,e^2/h$ and $G_{L_1R_3} \approx 0.60\,e^2/h$, whereas $G_{L_1R_2}$ is vanished, which is independent of the Néel domain wall configurations [see Figs. 19(e) and 19(g)]. One can also observe that the edge states are distributed at the boundaries of the odd-number layers equally from the LDOS [see Figs. 19(f) and 19(h)].

[1] Z. Qiao, J. Jung, C. Lin, Y. F. Ren, A. H. MacDonald, and Q. Niu, Phys. Rev. Lett. **112**, 206601 (2014).

[2] I. Martin, Y. M. Blanter, and A. F. Morpurgo, Phys. Rev. Lett. **100**, 036804 (2008).

[3] J. Jung, F. Zhang, Z. Qiao, and A. H. MacDonald, Phys. Rev. B **84**, 075418 (2011).

[4] S. G. Cheng, H. Liu, H. Jiang, Q. F. Sun, and X. C. Xie, Phys. Rev. Lett. **121**, 156801 (2018).

[5] Z. Qiao, J. Jung, Q. Niu, and A. H. MacDonald, Nano Lett. **11**, 3453 (2011).

[6] H. Pan, X. Li, F. Zhang, and S. A. Yang, Phys. Rev. B **92**, 041404(R) (2015).

[7] M. Wang, L. Liu, C.-C. Liu, and Y. Yao, Phys. Rev. B **93**, 155412 (2016).

[8] Y. Ren, J. Zeng, K. Wang, F. Xu, and Z. Qiao, Phys. Rev. B **96**, 155445 (2017).

[9] K. Wang, T. Hou, Y. Ren, and Z. Qiao, Front. Phys. **14**, 23501 (2019).

[10] Y. Han, S. You, and Z. Qiao, Phys. Rev. B **105**, 155301 (2022).

[11] T. Hou, G. Cheng, W.-K. Tse, C. Zeng, and Z. Qiao, Phys. Rev. B **98**, 245417 (2018).

[12] J. R. Anglin and A. Schulz, Phys. Rev. B **95**, 045430 (2017).

[13] C. Lee, G. Kim, J. Jung, and H. Min, Phys. Rev. B **94**, 125438 (2016).

[14] M. Yan, J. Lu, F. Li, W. Deng, X. Huang, J. Ma, and Z. Liu, Nat. Mater. **17**, 993 (2018).

[15] D. Xiao, W. Yao, and Q. Niu, Phys. Rev. Lett. **99**, 236809 (2007).

[16] F. Zhang, A. H. MacDonald, and E. J. Mele, Proc. Natl. Acad. Sci. USA **110**, 10546 (2013).

[17] J. Li, R. Zhang, Z. Yin, J. Zhang, K. Watanabe, T. Taniguchi, C. Liu, and J. Zhu, Science **362**, 1149 (2018).

[18] J. Li, K. Wang, Kenton J. McFaul, Z. Zern, Y. F. Ren, K. Watanabe, T. Taniguchi, Z. Qiao, and J. Zhu, Nat. Nanotechnol. **11**, 1060 (2016).

[19] M. Kim, J. H. Choi, S. H. Lee, K. Watanabe, T. Taniguchi, S. H. Jhi, and H. J. Lee, Nat. Phys. **12**, 1022 (2016).

[20] L. Ju, Z. Shi, N. Nair, Y. Lv, C. Jin, J. Velasco, Jr., H. A. Bechtel, M. C. Martin, A. Zettl, J. Analytis, and F. Wang, Nature (London) **520**, 650 (2015).

[21] L. J. Yin, H. Jiang, J. B. Qiao, and L. He, Nat. Commun. **7**, 11760 (2016).

[22] A. Gao, Y.-F. Liu, C. Hu, J.-X. Qiu, C. Tzschaschel, B. Ghosh, S.-C. Ho, D. Bérubé, R. Chen, H. Sun *et al.*, Nature (London) **595**, 521 (2021).

[23] M. M. Otrokov, I. I. Klimovskikh, H. Bentmann, D. Estyunin, A. Zeugner, Z. S. Aliev, S. Gaß, A. U. B. Wolter, A. V. Koroleva, A. M. Shikin *et al.*, Nature (London) **576**, 416 (2019).

[24] M. M. Otrokov, I. P. Rusinov, M. Blanco-Rey, M. Hoffmann, A. Yu. Vyazovskaya, S. V. Eremeev, A. Ernst, P. M. Echenique, A. Arnau, and E. V. Chulkov, Phys. Rev. Lett. **122**, 107202 (2019).

[25] I. I. Klimovskikh, M. M. Otrokov, D. Estyunin, S. V. Eremeev, S. O. Filnov, A. Koroleva, E. Shevchenko, V. Voroshnin, A. G. Rybkin, I. P. Rusinov *et al.*, npj Quantum Mater. **5**, 54 (2020).

[26] J. Li, C. Wang, Z. Zhang, B.-L. Gu, W. Duan, and Y. Xu, Phys. Rev. B **100**, 121103(R) (2019).

[27] J. H. Li, Y. Li, S. Q. Du, Z. Wang, B. L. Gu, S. C. Zhang, K. He, W. H. Duan, and Y. Xu, Sci. Adv. **5**, eaaw5685 (2019).

[28] Y.-J. Hao, P. Liu, Y. Feng, X.-M. Ma, E. F. Schwier, M. Arita, S. Kumar, C. Hu, R. Lu, M. Zeng *et al.*, Phys. Rev. X **9**, 041038 (2019).

[29] J. Ge, Y. Liu, J. Li, H. Li, T. Luo, Y. Wu, Y. Xu, and J. Wang, Natl. Sci. Rev. **7**, 1280 (2020).

[30] Y. Han, S. Sun, S. Qi, X. Xu, and Z. Qiao, Phys. Rev. B **103**, 245403 (2021).

[31] J. Li, J. Y. Ni, X. Y. Li, H. J. Koo, M. H. Whangbo, J. S. Feng, and H. J. Xiang, Phys. Rev. B **101**, 201408(R) (2020).

[32] P. M. Sass, W. Ge, J. Yan, D. Obeysekera, J. J. Yang, and W. Wu, Nano Lett. **20**, 2609 (2020).

[33] P. Swatek, Y. Wu, L.-L. Wang, K. Lee, B. Schrunk, J. Yan, and A. Kaminski, Phys. Rev. B **101**, 161109(R) (2020).

[34] Y. Hu, L. Xu, M. Shi, A. Luo, S. Peng, Z. Y. Wang, J. J. Ying, T. Wu, Z. K. Liu, C. F. Zhang *et al.*, Phys. Rev. B **101**, 161113(R) (2020).

[35] D. Zhang, M. Shi, T. Zhu, D. Xing, H. Zhang, and J. Wang, Phys. Rev. Lett. **122**, 206401 (2019).

[36] H. Sun, B. Xia, Z. Chen, Y. Zhang, P. Liu, Q. Yao, H. Tang, Y. Zhao, H. Xu, and Q. Liu, Phys. Rev. Lett. **123**, 096401 (2019).

[37] H.-P. Sun, C. M. Wang, S.-B. Zhang, R. Chen, Y. Zhao, C. Liu, Q. Liu, C. Chen, H.-Z. Lu, and X. C. Xie, Phys. Rev. B **102**, 241406(R) (2020).

[38] B. Lian, Z. Liu, Y. Zhang, and J. Wang, Phys. Rev. Lett. **124**, 126402 (2020).

[39] I. P. Rusinov, V. N. Men'shov, and E. V. Chulkov, Phys. Rev. B **104**, 035411 (2021).

[40] N. B. Devlin, T. Ferrus, and C. H. W. Barnes, Phys. Rev. B **104**, 054433 (2021).

[41] C. Xiao, J. Tang, P. Zhao, Q. Tong, and W. Yao, Phys. Rev. B **102**, 125409 (2020).

[42] N. Varnava, J. H. Wilson, J. H. Pixley, and D. Vanderbilt, Nat. Commun. **12**, 3998 (2021).

[43] S. Li, M. Gong, S. Cheng, H. Jiang, and X. Xie, arXiv:2207.09186.

[44] M. Gong, H. Liu, H. Jiang, C.-Z. Chen, and X. Xie, Natl. Sci. Rev., nwad025 (2023).

[45] A. Bernevig, T. Hughes, and S. C. Zhang, Science **314**, 1757 (2006).

[46] H. Zhang, C.-X. Liu, X.-L. Qi, X. Dai, Z. Fang, and S.-C. Zhang, Nat. Phys. **5**, 438 (2009).

[47] H. Jiang, Z. Qiao, H. Liu, and Q. Niu, Phys. Rev. B **85**, 045445 (2012).

[48] S. Datta, *Electronic Transport in Mesoscopic Systems* (Cambridge University Press, Cambridge, 1997).

[49] Z. Qiao, S. A. Yang, W. Feng, W. K. Tse, J. Ding, Y. Yao, J. Wang, and Q. Niu, Phys. Rev. B **82**, 161414(R) (2010).

[50] I. Purnama, I. S. Kerk, G. J. Lim, and W. S. Lew, Sci. Rep. **5**, 8754 (2015).

[51] Y.-F. Zhou, Z. Hou, and Q.-F. Sun, Phys. Rev. B **98**, 165433 (2018).

[52] J.-Z. Fang, S. Wang, X.-G. Ye, B.-C. Lin, A.-Q. Wang, H.-N. Cui, J.-K. Wang, G.-Y. Zhu, S. Liu, Y. Li *et al.*, Phys. Rev. B **104**, 054409 (2021).